An Effective Immuno-PET Imaging Method to Monitor CD8-Dependent Responses to Immunotherapy

Richard Tavaré[1,2], Helena Escuin-Ordinas[3], Stephen Mok[2], Melissa N. McCracken[2], Kirstin A. Zettlitz[1,2], Felix B. Salazar[1,2], Owen N. Witte[2,4,5,6], Antoni Ribas[2,3,7,8,9], and Anna M. Wu[1,2,7]

Abstract

The rapidly advancing field of cancer immunotherapy is currently limited by the scarcity of noninvasive and quantitative technologies capable of monitoring the presence and abundance of $CD8^+$ T cells and other immune cell subsets. In this study, we describe the generation of ^{89}Zr-desferrioxamine–labeled anti-CD8 cys-diabody (^{89}Zr-malDFO-169 cDb) for noninvasive immuno-PET tracking of endogenous $CD8^+$ T cells. We demonstrate that anti-CD8 immuno-PET is a sensitive tool for detecting changes in systemic and tumor-infiltrating CD8 expression in preclinical syngeneic tumor immunotherapy models including antigen-specific adoptive T-cell transfer, agonistic antibody therapy (anti-CD137/4-1BB), and checkpoint blockade antibody therapy (anti–PD-L1). The ability of anti-CD8 immuno-PET to provide whole body information regarding therapy-induced alterations of this dynamic T-cell population provides new opportunities to evaluate antitumor immune responses of immunotherapies currently being evaluated in the clinic. *Cancer Res; 76(1); 73–82. ©2015 AACR.*

Introduction

The rapidly evolving fields of tumor immunology and cancer immunotherapy have recently led to the FDA approval of several new immunotherapies, and many more therapies are presently in clinical trials for a variety of cancers. Furthermore, cellular, small molecule, antibody-based immunotherapies, and combinations thereof, are being rigorously tested preclinically for clinical translation. The dynamic tumor microenvironment and tumor heterogeneity have become important topics in both preclinical and clinical studies (1–3) but the ability to monitor changes in the immune status of metastatic cancers is limited. Current methods to monitor lymphocytes from whole blood or biopsies from heterogeneous tumors do not reflect the dynamic and spatial information required to monitor immune responses to therapeutic intervention, many of which elicit whole body changes in immune cell numbers and localization. Therefore, molecular imaging methods that can noninvasively monitor both systemic and intratumoral alterations in immune cell numbers or localization during experimental therapies have the ability to increase the understanding of the dynamics of immunotherapeutic mechanism with the potential to provide translatable methods for predicting and/or assessing clinical immunotherapeutic responses.

Analysis of tumor-infiltrating lymphocytes (TIL) has demonstrated the importance of tumor immune microenvironment and that the presence of cytotoxic $CD8^+$ T cells can predict overall survival in breast, lung, ovarian, melanoma, and colorectal cancers (reviewed in refs. 4 and 5). With the recent clinical successes of immunotherapies that alter the tumor immune microenvironment, including adoptive cell transfer (ACT) of T-cell receptor (TCR)- or chimeric antigen receptor-transduced cytotoxic T cells (6, 7), agonistic antibodies targeting CD137 (4-1BB) and CD40 (8–10), and antibody blockade of the checkpoint inhibitors CTLA-4 and PD-1/-L1 (11–13), the ability to noninvasively monitor the tumor immune response to therapy has become of upmost importance.

With this in mind, we have engineered an anti-CD8 antibody fragment (dimer of scFv or cys-diabody; cDb) from the parental rat anti-mouse CD8α YTS169.4.2.1 hybridoma (14) for noninvasive immuno-PET tracking of cytotoxic T cells in murine models of cancer immunotherapy. Immuno-PET combines the specificity and affinity of antibodies with the sensitivity of PET for whole body, quantitative, and noninvasive detection target antigens *in vivo* (15–17). Intact antibodies are engineered into antibody

[1]Crump Institute for Molecular Imaging, University of California Los Angeles, Los Angeles, California. [2]Department of Molecular and Medical Pharmacology, University of California Los Angeles, Los Angeles, California. [3]Department of Medicine, Division of Hematology-Oncology, University of California Los Angeles, Los Angeles, California. [4]Howard Hughes Medical Institute, University of California Los Angeles, Los Angeles, California. [5]Department of Microbiology, Immunology and Molecular Genetics, University of California Los Angeles, Los Angeles, California. [6]Eli and Edythe Broad Center of Regenerative Medicine and Stem Cell Research, University of California Los Angeles, Los Angeles, California. [7]Jonsson Comprehensive Cancer Center, University of California Los Angeles, Los Angeles, California. [8]Surgery, Division of Surgical Oncology, University of California Los Angeles, Los Angeles, California. [9]Institute for Molecular Medicine, David Geffen School of Medicine, University of California Los Angeles, Los Angeles, California.

Note: Supplementary data for this article are available at Cancer Research Online (http://cancerres.aacrjournals.org/).

Corresponding Authors: Richard Tavaré, California Nanosystems Institute 4350B, University of California, Los Angeles, 570 Westwood Plaza, Los Angeles, CA 90095-1770. Phone: 310-267-2819; Fax: 310-206-8975; E-mail: rtavare@mednet.ucla.edu; and Anna M. Wu, California Nanosystems Institute 4335, University of California, Los Angeles, 570 Westwood Plaza, Los Angeles, CA 90095-1770. Phone: 310-794-5088; Fax: 310-206-8975; E-mail: awu@mednet.ucla.edu

AACR 73

fragments such as the cDb (Fig. 1A) and minibody (dimer of scFv-C_H3; Mb) to enhance imaging characteristics, such as rapid clearance for high target-to-background images at short times after injection, reduced radiation dose, engineered sites for site-specific conjugation, and the removal of Fc effector functions, among others (17, 18).

The 169 cDb was engineered because it binds to CD8α (Lyt2) expressed on cytotoxic lymphocytes of all mouse strains so it can be used across murine immunotherapy models, unlike the previously developed 2.43 antibody fragments that bind cytotoxic T lymphocytes in Lyt2.2$^+$ mice (Balb/c and C57BL/6) but not Lyt2.1$^+$ mice (AKR and C3H; refs. 19, 20). Here, we assess the immuno-PET capabilities of the newly developed 169 cDb to bind to CD8 in vivo when radiolabeled with ^{89}Zr using the bifunctional chelator maleimide-DFO (^{89}Zr-malDFO-169 cDb) initially using wild-type mice and CD8-blocking studies. Subsequently, we tested the targeting capabilities of ^{89}Zr-malDFO-169 cDb to tumor-infiltrating CD8$^+$ T cells in three syngeneic murine models of immunotherapy: (i) ACT of antigen-specific T cells (OT-I) to mice bearing antigen-positive and antigen-negative EL4 tumors; (ii) agonistic antibody therapy (anti-CD137/4-1BB) for the treatment of CT26 colorectal tumors; and (iii) checkpoint blockade antibody therapy (anti–PD-L1) for the treatment of CT26

colorectal tumors. These models demonstrate not only the capabilities of anti-CD8 immuno-PET to target tumor-infiltrating CD8$^+$ T cells, but also provide insight into the systemic alterations of CD8$^+$ T cells that is characteristic to the immunotherapeutic mechanism of action.

Materials and Methods

C57BL/6, Balb/c, AKR, and OT-I mice were obtained from the Jackson Laboratories and housed and maintained by the Department of Laboratory Animal Medicine at the University of California, Los Angeles (UCLA). The UCLA Chancellor's Animal Research Committee approved protocols for all animal studies. Information regarding the construction of the anti-CD8 169 cDb and routine protein expression and purification, conjugations, ^{89}Zr radiolabeling, immunoreactivity, micro-PET acquisition, biodistribution, and data analysis can be found in the Supplementary Information.

Dendritic cell generation

The development of dendritic cells (DC) from murine bone marrow (BM) progenitor cells was performed as previously published (21). BM cells were cultured overnight in RPMI 1640 (Life
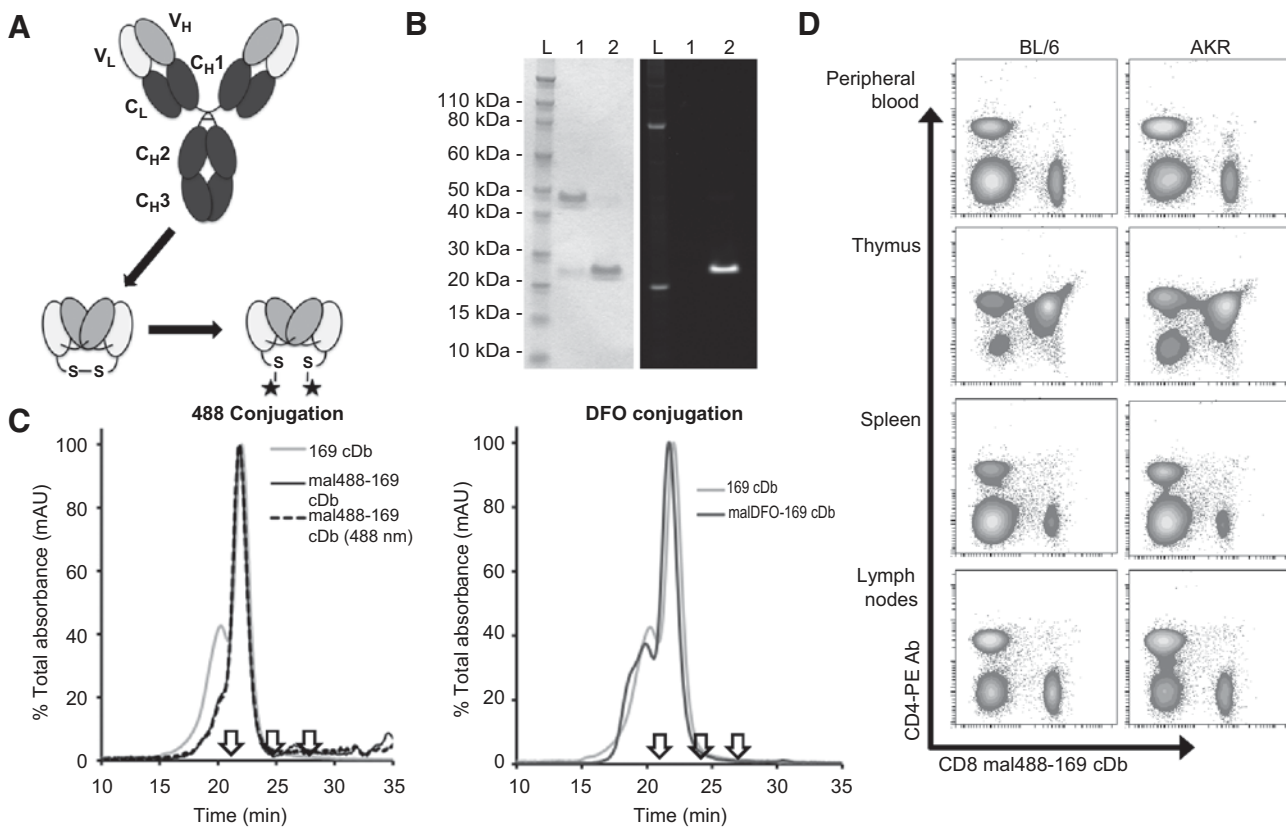

Figure 1.
Anti-CD8 169 cDb characterization. A, antibody engineering schematic of cys-diabody construction and site-specific conjugation to the engineered thiols. V_L and V_H are variable light and heavy chains, respectively. C_H1–3 are the heavy chain constant domains 1–3 and C_L is the light chain constant domain. B, SDS-PAGE gel (left) shows purified 169 cDb (Lane 1) and reduced and mal488-conjugated 169 cDb (lane 2) for fluorescent flow cytometry cell binding assays. The UV image (right) of the same gel shows mal488 conjugated to 169 cDb. C, size exclusion chromatography demonstrated the site-specific conjugation to mal488 had not disrupted the diabody confirmation (left). Site-specific conjugation to malDFO resulted in a similar size exclusion profile (right). Reference arrows indicate albumin (66 kDa) at 20.8 minutes, carbonic anhydrase (29 kDa) at 24.7 minutes, and cytochrome C (12.4 kDa) at 27.4 minutes. D, flow cytometry using the mal488-169 cDb of single cell suspensions from the blood, thymus, spleen, and lymph nodes of C57BL/6 (Lyt2.2$^+$; left column) and AKR (Lyt2.1$^+$; right column) mice.

Technologies) with 10% FCS, 1% penicillin, streptomycin, and amphotericin in a Petri dish. Nonadherent cells were re-plated on day 1 at 1×10^5 cells/well in 6-well plates with murine IL4 (500 U/mL; R&D Systems) and murine GM-CSF (100 ng/mL; Amgen) for 7 days. DC were resuspended at 2 to 5×10^6 cells/mL in serum-free RPMI and pulsed with $OVA_{257-264}$ peptide (AnaSpec) at a concentration of 10 μmol/L in serum-free media for 90 minutes at room temperature.

OT-I T-cell expansion

OT-1 splenocytes are harvested from OT-1 mice followed by 3 days of *ex vivo* activation with 100 U/mL IL2 and 1 μg/mL $OVA_{257-264}$ peptide. Then, the activated OT-1 splentocytes were expanded with 100 U/mL IL2 for the following 2 days before ACT.

EL4/EL4-Ova tumor model

C57BL/6 mice received total body irradiation of 900 cGy and then received 6×10^6 freshly isolated BM cells from another healthy C57BL/6 mouse. Two days later, mice were injected subcutaneously (s.c.) with either 5×10^5 EL4-Ova or EL4 into the right or left shoulders, respectively. On day 5 after tumor inoculations when tumors are approximately 5 mm in diameter, mice received 4.5×10^6 *ex vivo* expanded and $OVA_{257-264}$ peptide-activated OT-I T cells and were vaccinated s.c. with 7.5×10^6 $OVA_{257-264}$ peptide-pulsed DC. The ACT was followed by three consecutive days of intraperitoneal IL2 administration (50,000 IU; Novartis). On day 5 after ACT, mice were injected with ^{89}Zr-radiolabeled malDFO-169 cDb for immuno-PET imaging and biodistribution the following day (22 hours after injection).

Anti-CD137 and anti–PD-L1 CT26 tumor model

Balb/c mice were injected s.c. with 1×10^6 CT26 cells in the shoulder. Starting on day 7 after inoculation when the tumors have an average tumor diameter of about 3 to 4 mm, mice were injected i.p. with 12.5 mg/kg of either anti-CD137 antibody (clone 3H3; BioXCell) or anti–PD-L1 (clone 10F.9G2; BioXCell) every other day for four treatments. On day 15 after tumor inoculation, mice were injected with ^{89}Zr-radiolabeled malDFO-169 cDb for immuno-PET imaging and biodistribution the following day (22 hours after injection). Average tumor diameter was calculated using calipers on days 7, 11, and 15 after tumor inoculation.

Flow cytometry

Flow cytometry was performed on cell suspensions from the spleen, peripheral blood, thymus, and lymph nodes. Mashing organs over 75-mm filters (BD Biosciences) in RPMI plus 5% FBS provided single cell suspensions. Following red blood cell lysis using ammonium chloride–potassium lysis buffer, the cells were stained for 1 hour on ice, washed with PBS, and analyzed using a BD FACSCanto. The following antibodies were used for staining: Alexa488-conjugated 169 cDb, anti–CD4-PE (clone GK1.5), anti–CD45-APC (clone 30-F11; all fluorescent Abs from eBioscience).

For tumor digestion to single cell suspensions, tumors were incubated with Collagenase (type I; Invitrogen) at 1 mg/mL in RPMI plus 5% FBS for 1 hour at 37°C with continual shaking followed by straining over a 75-mm filter. The following antibodies were used for staining: anti–CD8-FITC (clone 53-6.7), anti–CD4-APC-Cy7 (clone GK1.5), anti–CD3-APC (clone 17A2),

and anti–CD45-PE (clone 30-F11; all fluorescent Abs from eBioscience).

Results

The engineered anti-CD8 169 cys-diabody retained binding to $CD8^+$ T cells

The anti-CD8 169 cys-diabody was engineered from the previously described anti-CD8 169 minibody (19) and was purified to >95% purity (Fig. 1B) with a yield of 9.2 mg/L cell culture supernatant. Size exclusion chromatography (SEC) confirmed the correct molecular weight of approximately 55 kDa with a small amount of higher molecular weight multimers (Fig. 1C).

The 169 cDb was conjugated site-specifically to maleimide-Alexa Fluor 488 (mal488) with a dye-to-protein molar ratio of 1.5:1 and a recovery of 55% after purification. The mal488 was covalently coupled to the monomeric 169 cDb as seen by fluorescence detection on the SDS-PAGE analysis (Fig. 1B). SEC profiles of both the mal488-169 cDb and native 169 cDb were very similar (Fig. 1C, left), indicating the conjugate retained its cross-paired dimeric diabody structure. Flow cytometry using the mal488-169 cDb on primary cells isolated from the peripheral blood, thymus, spleen, and lymph nodes from both $Lyt2.2^+$ C57BL/6 and $Lyt2.1^+$ AKR mice demonstrated that the engineered cDb retains the ability to bind CD8α expressed on all mouse strains (Fig. 1D).

^{89}Zr-radiolabeled anti-CD8 169 cDb specifically targets $CD8^+$ T cells *in vivo* as detected by immuno-PET

Similar to mal488 conjugation, the site-specific maleimide-DFO (malDFO) conjugation to the 169 cDb did not disrupt the diabody bivalent conformation as shown by SEC (Fig. 1C, right). The ^{89}Zr radiolabeling efficiency, radiochemical purity, specific activity, protein dose injected, and immunoreactivity are reported in Table 1.

In order to test for CD8 specificity *in vivo*, ^{89}Zr-malDFO-169 cDb was injected into either wild-type AKR mice or CD8-blocked AKR mice that received a bolus co-injection of 3 mg/kg (~60 μg) nonradiolabeled 169 cDb (Fig. 2A). Immuno-PET acquisition at 4, 8, and 22 hours after injection demonstrated specific targeting to the spleen and lymph nodes in unblocked mice as early as 4 hours after injection, clearance from the circulation over time, and high contrast images at 22 hours after injection. Transverse CT and PET/CT images demonstrated targeting to the inguinal lymph nodes and spleen of wild-type mice (Fig. 2B). *Ex vivo* biodistribution of wild-type and CD8-blocked mice confirmed CD8 specificity *in vivo* and significantly decreased uptake in lymphoid organs of CD8-blocked mice (Fig. 2C and Supplementary Table S1).

Table 1. ^{89}Zr-malDFO-169 cDb radiolabeling, protein dose, and immunoreactivity characteristics

	Average	Range
Radiolabeling efficiency	98.3 ± 1.1%	97–99.8%
Radiochemical purity	99.5 ± 0.4%	99–99.9%
Specific activity	4.27 ± 0.5 μCi/μg (158 ± 18 kBq/μg)	3.5–4.9 μCi/μg (129–181 kBq/μg)
Protein dose injected	10.2 ± 0.9 μg	9.4–12.2 μg
Immunoreactivity	86.6 ± 1.6%	84.9–88.1%

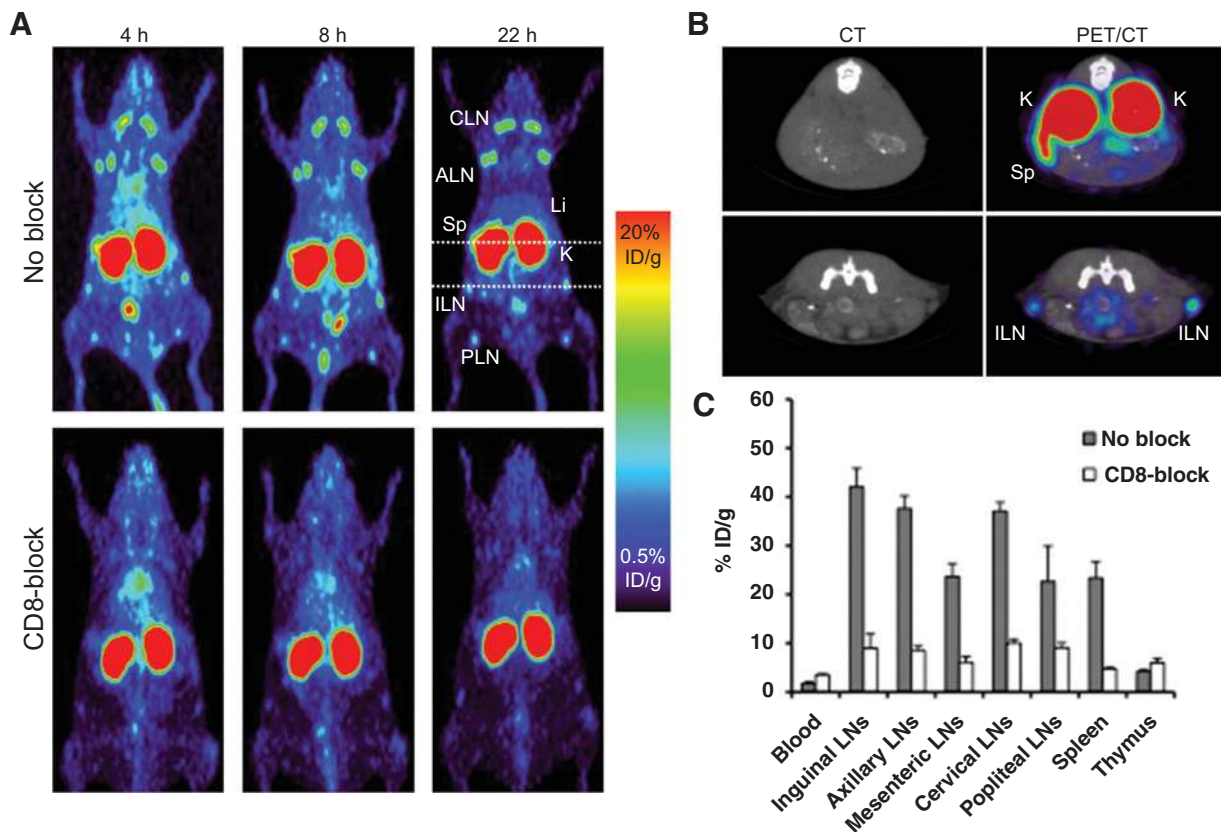NOTE: $n = 8$ except for immunoreactivity, where $n = 3$.

Figure 2.
Anti-CD8 micro-PET of ^{89}Zr-malDFO-169 cDb in wild-type and CD8-blocked AKR mice. A, ^{89}Zr-malDFO-169 cDb was injected into wild-type (top) and CD8-blocked (bolus 3 mg/kg GK1.4 cDb; bottom) AKR mice and imaged at 4, 8, and 22 hours after injection. Images are represented as 25 mm maximum intensity projections. B, transverse CT and PET/CT images indicated with dashed white bars show specific targeting to the spleen and lymph nodes of wild-type AKR mice. C, *ex vivo* biodistribution at 22 hours after injection of ^{89}Zr-malDFO-169 cDb from wild-type and CD8-blocked AKR mice (n = 3 per group). CLN, cervical lymph node; ALN, axillary lymph node; Li, liver; Sp, spleen; K, kidney; ILN, inguinal lymph node; PLN, popliteal lymph node.

Anti-CD8 immuno-PET detects antigen-specific tumor targeting of adoptively transferred T cells

ACT therapy is based on the infusion of a large number of tumor antigen-specific T cells. We reasoned that this treatment approach would be a suitable initial platform to test the ability of ^{89}Zr-malDFO-169 cDb to detect TILs using anti-CD8 immuno-PET. C57BL/6 mice bearing s.c. EL4 and EL4-Ova tumors were injected with CD8$^+$ T cells expressing the MHC-I-restricted TCR specific for OVA isolated from OT-I mice (Fig. 3A). Five days after adoptive T cell therapy (ACT), the tumor-bearing mice were injected with ^{89}Zr-malDFO-169 cDb and imaged 22 hours after injection (Fig. 3B). Anti-CD8 immuno-PET detected increased uptake in the EL4-Ova tumor compared with the antigen-negative EL4 tumor that was confirmed by *ex vivo* biodistribution (Fig. 3B and C and Supplementary Table S2). Transverse images showed distribution of activity throughout the EL4-Ova tumor and only diffuse uptake in the antigen-negative EL4 tumor (Fig. 3C, bottom and Supplementary Fig. S1). Interestingly, uptake in the draining axillary lymph node of the EL4-Ova tumor was the highest of all lymphoid organs and is detectable by immuno-PET even though s.c. dorsal DC vaccination, combined with high dose IL2 therapy, was expected to cause inguinal lymph node detection due to antigen-specific T-cell proliferation (Supplementary Fig. S1). Inguinal lymph nodes have decreased in size compared with wild-type mice due to whole body irradiation, reflecting a reduction in total lymphocyte numbers, and have decreased uptake compared with wild-type mice in *ex vivo* biodistribution (Supplementary Fig. S2 and Supplementary Table S2).

CD8-blocked tumor-bearing mice showed similar uptake in both tumors (Fig. 3B, right) and decreased uptake to the lymph nodes and spleen (Fig. 3C). Increased ratios of EL4-Ova:EL4, EL4-Ova:blood, and EL4:blood of CD8-unblocked compared with CD8-blocked mice confirmed CD8-specific targeting to the Ova expressing tumor (Fig. 3D). Flow cytometry analysis of harvested tumors confirmed significant increase of CD45$^+$CD8$^+$ T cells in the antigen-positive EL4-Ova tumor compared with the antigen-negative EL4 tumor (Fig. 3E). Importantly, anti-CD8 immuno-PET demonstrated specific detection of CD8$^+$ T cells in the EL4-Ova tumor of antigen-specific adoptively transferred cytotoxic lymphocytes.

Anti-CD8 immuno-PET detects tumor-infiltrating CD8$^+$ T cells after agonistic anti-CD137 immunotherapy

We then tested the ability of ^{89}Zr-malDFO-169 cDb immuno-PET to image endogenous T-cell responses to cancer induced by immune-activating antibody therapy. Balb/c mice bearing s.c. CT26 tumors underwent agonistic anti-CD137 antibody therapy (Fig. 4A) that induced tumor regression (Fig. 4B) as demonstrated previously (22). ^{89}Zr-malDFO-169 cDb immuno-PET of
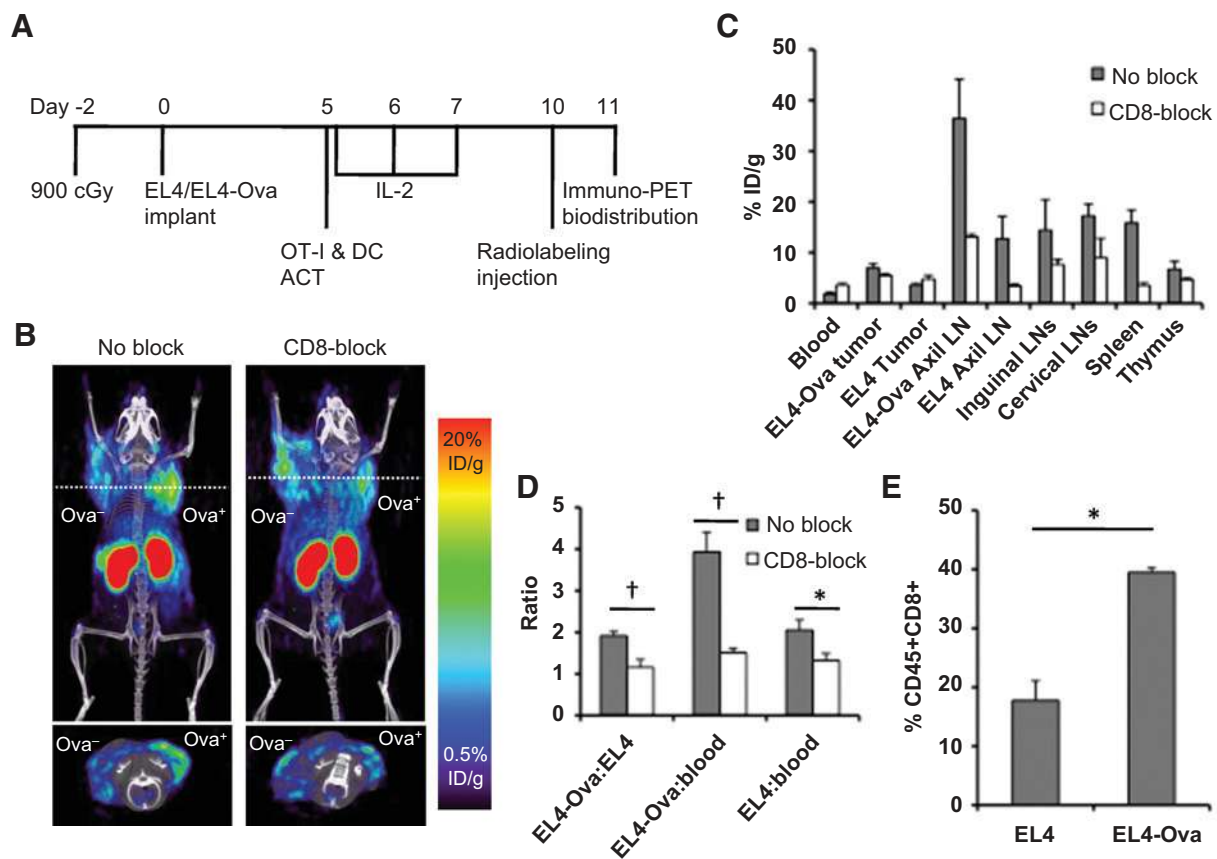
Figure 3.
Anti-CD8 immuno-PET of ^{89}Zr-malDFO-169 cDb in the OT-I adoptive T-cell therapy model. A, C57BL/6 mice bearing s.c. EL4 and EL4-Ova tumors received the full protocol of myelodepletion (900 cGy) with hematopoietic stem cell (HSC)/BM transplantation, adoptive OT-I T cell transfer followed by OVA-pulsed DC vaccination and high dose IL2. B, representative immuno-PET images at 22 hours after injection of ^{89}Zr-malDFO-169 cDb of unblocked and CD8-blocked mice bearing EL4-Ova and EL4 tumors 5 days after adoptive OT-I T cell transfer. Coronal images are presented as 25 mm maximum intensity projections and transverse images are presented as 2 mm maximum intensity projections. C, *ex vivo* biodistribution at 22 hours after injection of ^{89}Zr-malDFO-169 cDb of unblocked and CD8-blocked mice bearing EL4-Ova and EL4 tumors ($n = 3$ per group). Full biodistribution analysis is in Supplementary Table S2. D, ratios of EL4-Ova:EL4, EL4-Ova:blood, and EL4:blood of unblocked and CD8-blocked mice from *ex vivo* biodistribution analysis. E, flow cytometry analysis of tumors harvested 5 days after adoptive T-cell therapy was used to determine the percentage of CD45^{+}CD8^{+} T cells in the antigen-positive EL4-Ova tumor versus the antigen-negative EL4 tumor ($n = 3$). *, $P < 0.05$; †, $P < 0.005$.

anti-CD137-treated mice showed higher intratumoral probe accumulation when compared with both anti-CD137-treated/CD8-blocked and untreated tumor-bearing mice that was validated by *ex vivo* biodistribution (Fig. 4C and E and Supplementary Table S3). Transverse images of anti-CD137-treated mice showed uptake throughout the tumor, indicating cytotoxic T-cell infiltration, although the CT26 tumors of untreated mice showed a peripheral rim of uptake around the tumor (Fig. 3C, bottom and Supplementary Fig. S3). IHC analysis of CD8 expression of CT26 tumors treated with anti-CD137 therapy confirmed the presence of CD8^{+} tumor-infiltrating T cells in tumors (Fig. 4D). IHC of untreated CT26 tumors showed the majority of the rim is CD8 negative but some CD8 staining can be detected at distinct locations, indicating that the rim uptake of ^{89}Zr-malDFO-169 cDb could be partially due to resident CD8^{+} T cells but also possibly due to nonspecific uptake resulting from ruptured vasculature and the enhanced permeability and retention effect (Supplementary Fig. S4).

Anti-CD8 immuno-PET and *ex vivo* biodistribution confirmed a significant increase of ^{89}Zr-malDFO-169 cDb uptake in lymphatic

organs of anti-CD137-treated mice compared with both anti-CD137-treated/CD8-blocked and untreated mice (Fig. 4C and E and Supplementary Table S3). Compared with the ACT model, agonistic anti-CD137 therapy caused a systemic increase in size of lymph nodes (about fivefold; Supplementary Fig. S2) as previously reported (23), resulting in enhanced detection of inguinal lymph nodes (Fig. 4C and Supplementary Fig. S3). Tumor-to-blood ratios of anti-CD137-treated, anti-CD137-treated/CD8-blocked, and control tumor-bearing mice confirmed CD8-specific targeting to the CD137-treated tumors (Fig. 4F). Flow cytometry analysis of harvested tumors confirmed significant increase of CD45^{+}CD8^{+} T cells in the anti-CD137-treated tumor compared with the untreated tumor (Fig. 4G).

Anti-CD8 immuno-PET detects tumor-infiltrating CD8^{+} T cells in mice responding to checkpoint blockade immunotherapy

It has been previously reported that 25% or 33% of Balb/c mice bearing CT26 s.c. implanted tumors demonstrated complete tumor regression in response to anti–PD-1 or anti–PD-L1 checkpoint blockade therapy, respectively, although nonresponding
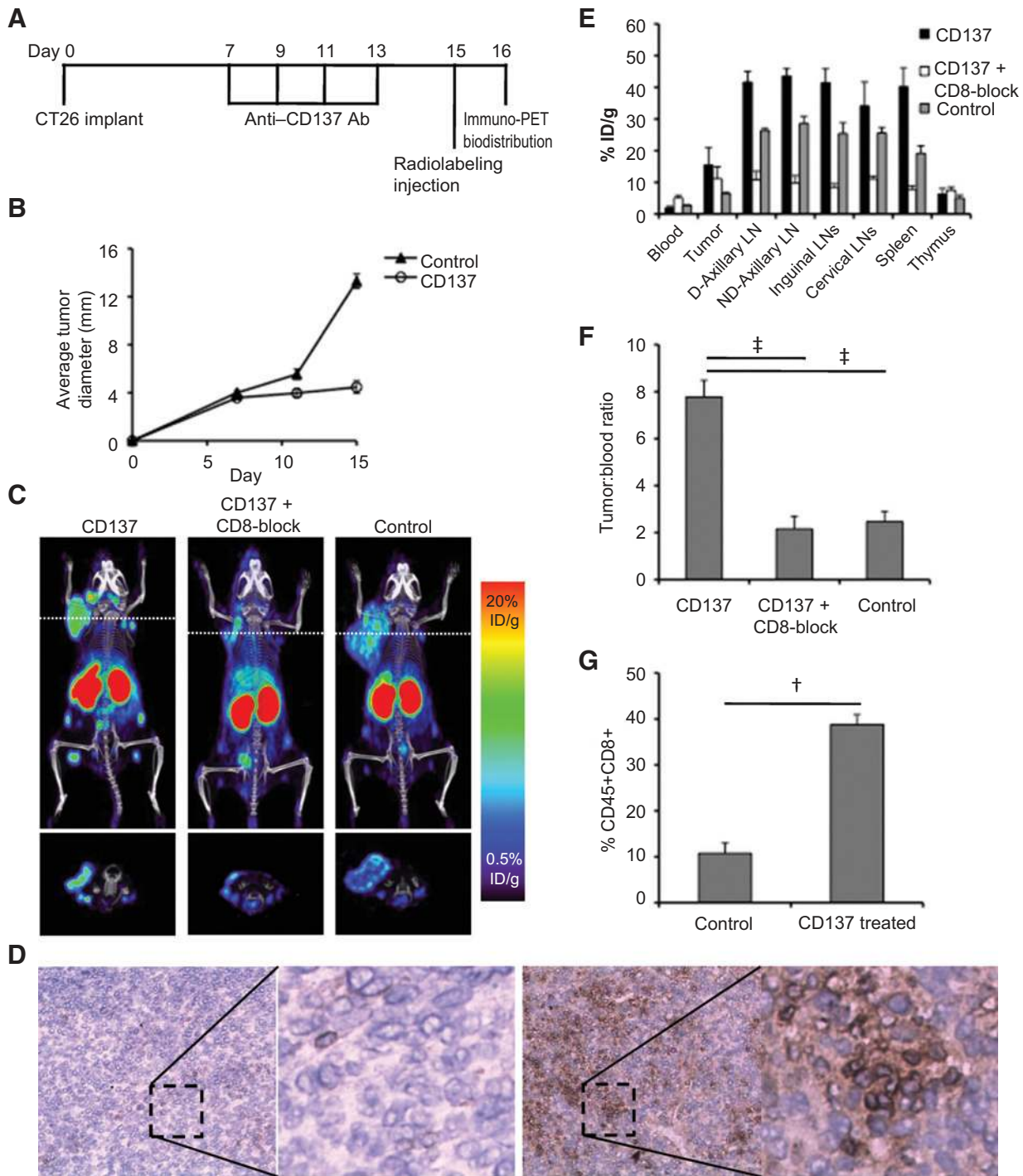
Figure 4.
Anti-CD8 immuno-PET of ^{89}Zr-malDFO-169 cDb in the CT26/anti-CD137 immunotherapy model. A, Balb/c mice bearing s.c. CT26 tumors were treated with anti-CD137 therapy every other day for four treatments and anti-CD8 immuno-PET was acquired on day 16 after tumor implantation. B, tumor growth curves of CD137 treated and untreated mice (average tumor diameter). C, on day 8 after immunotherapy initiation, CD137-treated mice, CD137-treated/CD8-blocked mice, and control mice (no anti-CD137 therapy) were injected with ^{89}Zr-malDFO-169 cDb and immuno-PET images were acquired at 22 hours after injection. D, CD8 IHC of untreated CT26 tumors or anti-CD137-treated CT26 tumors indicate the presence of increased CD8^{+} tumor-infiltrating lymphocytes. E, ex vivo biodistribution at 22 hours after injection of ^{89}Zr-malDFO-169 cDb of CD137-treated mice, CD137-treated/CD8-blocked mice, and control mice ($n = 3$ per group). Full biodistribution analysis is in Supplementary Table S3. F, tumor-to-blood ratios of CD137-treated mice, CD137-treated/CD8-blocked mice, and control mice. G, flow cytometry analysis of tumors harvested on day 15 was used to determine the percentage of CD45^{+}CD8^{+} T cells in the CT26 tumors ($n = 3$). †, $P < 0.005$; ‡, $P < 0.0005$.

mice showed tumor progression (24). In our study, Balb/c mice bearing week old CT26 tumors underwent anti–PD-L1 checkpoint blockade therapy (Fig. 5A) and were segregated into two groups termed responders (<8 mm avg. tumor diameter) and nonresponders (>8 mm avg. tumor diameter) at day 14 after tumor inoculation (Fig. 5B). Similar to previous reports (24), about 25% of treated mice showed delayed tumor progression at day 14.

^{89}Zr-malDFO-169 cDb immuno-PET of anti–PD-L1 responders showed higher tumor uptake when compared with tumors of anti–PD-L1 nonresponders that was confirmed by *ex vivo* biodistribution (Fig. 5C and D and Supplementary Table S4). Similar to the CT26/anti-CD137 therapy model, transverse images demonstrated distinct intratumoral probe uptake in anti–PD-L1–

responding mice, indicating the presence of intratumoral CD8$^+$ T cells and a peripheral rim of activity in anti–PD-L1–nonresponding mice (Fig. 5C, bottom and Supplementary Fig. S5). Unlike anti-CD137 therapy that demonstrated enhanced inguinal lymph node detection, anti–PD-L1 responders and nonresponders did not show enhanced detection of CD8$^+$ T lymphocytes in the inguinal lymph nodes (Fig. 5C) but the inguinal lymph nodes doubled in size (Supplementary Fig. S2).

Compared with the ACT and anti-CD137 therapy models, the tumor-to-blood ratio of the mice that responded to anti–PD-L1 therapy was insignificant when compared with nonresponders (Fig. 5E) even though analysis of harvested tumors confirmed an increase of CD45$^+$CD8$^+$ T cells in the tumors responding to anti–PD-L1 therapy compared with nonresponding and control
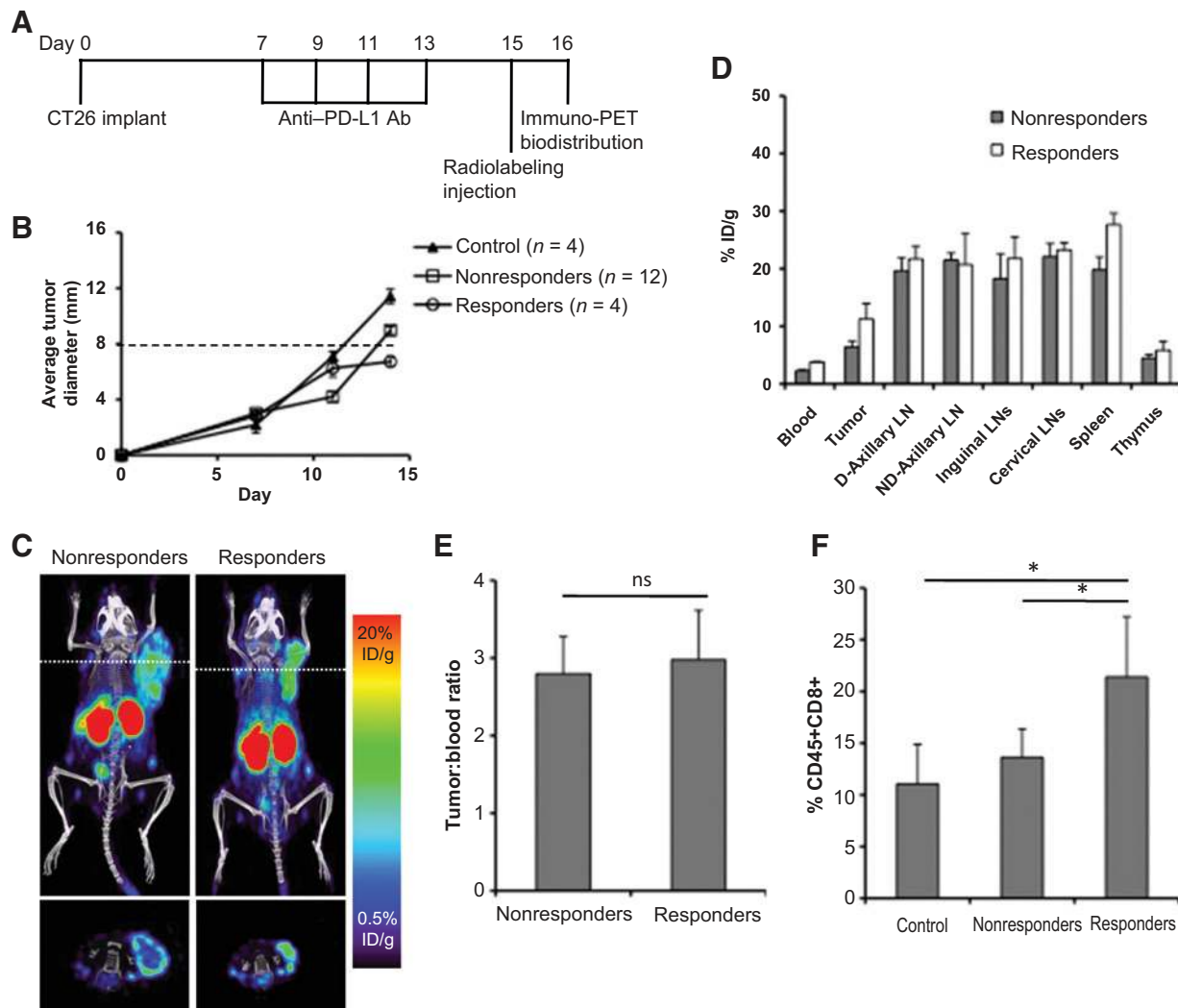

Figure 5.
Anti-CD8 immuno-PET of ^{89}Zr-malDFO-169 cDb in the CT26/anti–PD-L1 immunotherapy model. A, Balb/c mice bearing s.c. CT26 tumors were treated with anti–PD-L1 therapy every other day for four treatments and anti-CD8 immuno-PET was acquired on day 16 after tumor implantation. B, tumor growth curves of control (no anti–PD-L1 therapy), partial responders to anti–PD-L1 therapy (tumor < 8 mm average diameter), and nonresponders to anti–PD-L1 therapy (tumor > 8 mm average diameter)-treated and untreated mice (average tumor diameter). C, representative ^{89}Zr-malDFO-169 cDb immuno-PET images acquired at 22 hours after injection of anti–PD-L1 responding and nonresponding mice. D, *ex vivo* biodistribution at 22 hours after injection of ^{89}Zr-malDFO-169 cDb of anti–PD-L1–responding and -nonresponding mice (n = 3–4 per group). Full biodistribution analysis is in Supplementary Table S4. E, tumor-to-blood ratios of anti–PD-L1–responding and -nonresponding mice. F, flow cytometry analysis of tumors harvested on day 15 was used to determine the percentage of CD45$^+$CD8$^+$ T cells in the CT26 tumors in control, anti–PD-L1–responding, and anti–PD-L1–nonresponding mice (n = 4–5). *, P < 0.05.

untreated tumors (Fig. 5F). Interestingly, probe uptake in the tumors of anti–PD-L1 nonresponders was similar to tumor uptake to control untreated CT26 tumors and the percentage of CD45^{+}CD8^{+} T cells was similar (Fig. 4D and F). Importantly, anti-CD8 immuno-PET was able to detect increased intratumoral CD8^{+} T lymphocytes in mice responding to checkpoint blockade therapy.

Discussion

In the present study, we demonstrate that anti-CD8 immuno-PET provides an integrated readout that is reflective of both systemic and intratumoral alterations in CD8^{+} T cell numbers due to three mechanistically different models of immunotherapy. For example, anti-CD8 immuno-PET detection of nontumor draining lymph nodes and the spleen in the ACT model is decreased, resulting from whole body irradiation, it is enhanced in the anti-CD137 model due to the systemic agonistic activity of the therapy on immune cells throughout the body, and does not change greatly for anti–PD-L1 therapy due to the restricted expression of PD-L1 on tumor cells and myeloid-derived suppressor cells within the tumor. The successful noninvasive imaging of CD8^{+} T cell responses to cancer was achieved by targeting a physiologically expressed surface molecule using a clinically compatible approach.

The [89]Zr-radiolabeled 169 cDb demonstrated specific targeting to CD8 in vivo as detected by immuno-PET. The engineered C-terminal cysteine allowed for site-specific conjugation of the bifunctional chelator maleimide-DFO away from the binding site of the cDb to avoid decreased immuno-reactivity upon conjugation. Importantly, the cDb retains its cross-paired, bivalent structure and does not form monovalent scFvs upon mild reduction and thiol-specific conjugation (25). Compared with the previously engineered 169 minibody fragment used for ^{64}Cu immuno-PET (19), the cDb showed less aggregation, slower blood clearance, and enhanced lymph node and spleen targeting at 22 hours after injection. The cDb exhibited high renal accumulation due to the lower molecular weight of the cys-diabody (∼55 kDa) compared with the minibody (∼80 kDa), the renal filtration cutoff of approximately 60 kDa, and the use of the residualizing radiometal [89]Zr.

Detecting small regions of interest using PET is inherently difficult due to the partial volume effect whereby activity in small regions of interest near or below the resolution of the scanner, such as lymph nodes, is underestimated (26). This underestimation varies due to scanner resolution and the positron range of the radionuclide used, but it can be compensated for using partial volume correction (26, 27). Even with this limitation, we have shown anti-CD8 immuno-PET can detect lymph nodes in wild-type mice and in a model of T-cell repopulation after hematopoietic stem cell transplant (19, 20).

Due to immunotherapy-induced alterations of CD8 expressed in the antigen sink, i.e., spleen and lymph nodes, the optimal protein dose will be dependent on the immunotherapeutic mechanism of action and the ability to consistently target intratumoral CD8^{+} T cells will rely on a fine balance between blocking the CD8 antigen sink and displacing tumor uptake. The importance of protein dose for tumor epitope targeting has been demonstrated previously where a natural antigen sink exists in imaging studies targeting HER2 (28), neuropilin-1 (29), and EGFR (30), and antibody-drug conjugate studies targeting TENB2

(31). A recent publication by Muylle and colleagues studying [89]Zr-rituximab immuno-PET in patients with CD20^{+} B-cell lymphomas demonstrates the importance of antigen sink and protein dose to obtain consistent lymphoma detection that will be relevant for reproducible anti-CD8 immuno-PET in the clinic (32). In the future, enhanced tumor-infiltrating CD8^{+} T cell targeting might be achieved in the models presented here by optimizing the anti-CD8 cys-diabody dose for each immunotherapy.

Anti-CD8 immuno-PET is a powerful method used to specifically monitor endogenous CD8^{+} T cells noninvasively without the need for ex vivo manipulation of lymphocytes. Direct radiolabeling of lymphocytes ex vivo allows for monitoring initial cell migration of adoptively transferred cells, but suffers from radionuclide half-life, probe dilution due to cell division and potential toxic effects of the radionuclide on radiosensitive lymphocytes (33–35). Reporter gene transduction of cells ex vivo benefits from signal amplification due to cell division, repeat monitoring, and longitudinal tracking of genetically engineered cells (36–39). However, reporter probes demonstrate high background in clearance organs and reporter genes require development of nonimmunogenic reporters for translation (37, 40). Small molecule metabolic probes that do not require ex vivo cellular manipulation, such as 2-deoxy-2-(^{18}F)-fluoro-D-glucose ([^{18}F]-FDG) and 1-(2′-deoxy-2′(^{18}F)fluoroarabinofuranosyl) cysteine ([^{18}F]-FAC), are either not specific for cytotoxic lymphocytes alone ([^{18}F]-FDG) or they target proliferating lymphocytes in secondary lymphoid organs and fail to detect TILs ([^{18}F]-FAC; ref. 41).

Anti-CD8 immuno-PET was able to detect tumor-infiltrating CD8^{+} T cell alterations in three immunotherapeutic models that have shown great promise in the clinic. The development of analogous imaging agents for human use would be of great utility, particularly in light of the recent advances in clinical immuno-oncology, including FDA approvals of checkpoint inhibitors such as ipilimumab, nivolumab, and pembrolizumab, and the bispecific blinatumomab for T-cell recruitment. A fully human imaging agent specific for human CD8 can be arrived at through humanization of existing anti-CD8 monoclonal antibodies or de novo isolation of fully human antibodies by phage display (42). Alternative scaffolds, such as single domain camelid antibodies labeled with ^{18}F or ^{64}Cu for PET, have demonstrated utility in the detection of the macrophage mannose receptors, MHC Class II, and CD11b expressed on myeloid cells in preclinical models (43, 44). However, such agents might require humanization to reduce potential immunogenicity. With any imaging agent specific for human CD8 T cells, preclinical testing would require the use of transgenic expressing human CD8 or humanized mouse models, such as NSG mice reconstituted with human peripheral blood mononuclear cells or CD34^{+} hematopoietic stem cells, which can be used to establish models of tumor immunotherapy. Furthermore, it will be essential to evaluate potential effects of administration on T cell viability, proliferation, and function in vivo. Finally, radiation dose estimates need to be calculated based on the biodistribution and time-activity curves of potential CD8 PET tracers in preclinical models, in order to determine appropriate levels of protein and radioactivity that can be administered to patients.

The potential utility of immuno-PET for imaging immune cell subsets in humans is supported by many previous clinical studies using radiolabeled intact antibodies targeting T and B lymphocytes for detection of inflammation in vivo using planar gamma imaging and single photon emission CT (45). In oncology,

gamma camera imaging of ^{131}I-tositumomab or ^{111}In-ibritumomab tiuxetan can be used to confirm CD20 targeting prior to or in conjugation with radioimmunotherapy (46). Success of these approaches for imaging immune cell subsets using intact antibodies suggests that the transition to bespoke engineered antibody fragments for immuno-PET should be feasible and favorable. Importantly, we believe immuno-PET monitoring of lymphocytes and other immune cell subsets could transform the ability to profile the tumor immune microenvironment and antitumor immune responses in the context of cancer immunotherapy in the clinic.

Disclosure of Potential Conflicts of Interest

R. Tavaré is a consultant for ImaginAb, Inc. A.M. Wu is a board member at ImaginAb, Inc.; has ownership interest (including patents) in ImaginAb, Inc.; and is a consultant/advisory board member for ImaginAb, Inc. Part of the technology described in this manuscript is licensed by the Regents of the University of California to ImaginAb, Inc. and the Regents have taken equity in ImaginAb, Inc. as part of the licensing transaction. No potential conflicts of interest were disclosed by the other authors.

Authors' Contributions

Conception and design: R. Tavaré, S. Mok, M.N. McCracken, O.N. Witte, A. Ribas, A.M. Wu
Development of methodology: R. Tavaré, S. Mok
Acquisition of data (provided animals, acquired and managed patients, provided facilities, etc.): R. Tavaré, H. Escuin-Ordinas, S. Mok, M.N. McCracken, K.A. Zettlitz, F.B. Salazar, A. Ribas
Analysis and interpretation of data (e.g., statistical analysis, biostatistics, computational analysis): R. Tavaré, H. Escuin-Ordinas, S. Mok, M.N. McCracken, K.A. Zettlitz, A.M. Wu

Writing, review, and/or revision of the manuscript: R. Tavaré, S. Mok, K.A. Zettlitz, O.N. Witte, A. Ribas, A.M. Wu
Administrative, technical, or material support (i.e., reporting or organizing data, constructing databases): K.A. Zettlitz, A. Ribas
Study supervision: R. Tavaré, A.M. Wu

References

1. Hanahan D, Weinberg RA. Hallmarks of cancer: the next generation. Cell 2011;144:646–74.
2. Mantovani A, Allavena P, Sica A, Balkwill F. Cancer-related inflammation. Nature 2008;454:436–44.
3. Schreiber RD, Old LJ, Smyth MJ. Cancer immunoediting: integrating immunity's roles in cancer suppression and promotion. Science 2011;331:1565–70.
4. Pages F, Galon J, Dieu-Nosjean MC, Tartour E, Sautes-Fridman C, Fridman WH. Immune infiltration in human tumors: a prognostic factor that should not be ignored. Oncogene 2010;29:1093–102.
5. Gooden MJ, de Bock GH, Leffers N, Daemen T, Nijman HW. The prognostic influence of tumour-infiltrating lymphocytes in cancer: a systematic review with meta-analysis. Br J Cancer 2011;105:93–103.
6. Johnson LA, Morgan RA, Dudley ME, Cassard L, Yang JC, Hughes MS, et al. Gene therapy with human and mouse T-cell receptors mediates cancer regression and targets normal tissues expressing cognate antigen. Blood 2009;114:535–46.
7. Rosenberg SA. Raising the bar: the curative potential of human cancer immunotherapy. Sci Transl Med 2012;4:127ps8.
8. Melero I, Grimaldi AM, Perez-Gracia JL, Ascierto PA. Clinical development of immunostimulatory monoclonal antibodies and opportunities for combination. Clin Cancer Res 2013;19:997–1008.
9. Melero I, Hervas-Stubbs S, Glennie M, Pardoll DM, Chen L. Immunostimulatory monoclonal antibodies for cancer therapy. Nat Rev Cancer 2007;7:95–106.
10. Vinay DS, Kwon BS. Immunotherapy of cancer with 4-1BB. Mol Cancer Ther 2012;11:1062–70.
11. Callahan MK, Wolchok JD. At the bedside: CTLA-4- and PD-1-blocking antibodies in cancer immunotherapy. J Leukoc Biol 2013;94:41–53.
12. Shin DS, Ribas A. The evolution of checkpoint blockade as a cancer therapy: what's here, what's next? Curr Opin Immunol 2015;33C:23–35.
13. Topalian SL, Drake CG, Pardoll DM. Immune checkpoint blockade: a common denominator approach to cancer therapy. Cancer Cell 2015;27:450–61.
14. Cobbold SP, Jayasuriya A, Nash A, Prospero TD, Waldmann H. Therapy with monoclonal antibodies by elimination of T-cell subsets in vivo. Nature 1984;312:548–51.
15. Wu AM. Antibodies and antimatter: the resurgence of immuno-PET. J Nucl Med 2009;50:2–5.
16. Knowles SM, Wu AM. Advances in immuno-positron emission tomography: antibodies for molecular imaging in oncology. J Clin Oncol 2012;30:3884–92.
17. Wu AM. Engineered antibodies for molecular imaging of cancer. Methods 2014;65:139–47.
18. Olafsen T, Wu AM. Antibody vectors for imaging. Semin Nucl Med 2010;40:167–81.
19. Tavaré R, McCracken MN, Zettlitz KA, Knowles SM, Salazar FB, Olafsen T, et al. Engineered antibody fragments for immuno-PET imaging of endogenous CD8+ T cells in vivo. Proc Natl Acad Sci U S A 2014;111:1108–13.
20. Tavaré R, McCracken MN, Zettlitz KA, Salazar FB, Olafsen T, Witte ON, et al. ImmunoPET of murine T cell reconstitution post-adoptive stem cell transplant using anti-CD4 and anti-CD8 cys-diabodies. J Nucl Med 2015;56:1258–64.
21. Prins RM, Shu CJ, Radu CG, Vo DD, Khan-Farooqi H, Soto H, et al. Antitumor activity and trafficking of self, tumor-specific T cells against tumors located in the brain. Cancer Immunol Immunother 2008;57:1279–89.
22. Escuin-Ordinas H, Elliott MW, Atefi M, Lee M, Ng C, Wei L, et al. PET imaging to non-invasively study immune activation leading to antitumor responses with a 4-1BB agonistic antibody. J Immunother Cancer 2013;1:14.
23. Schrand B, Berezhnoy A, Brenneman R, Williams A, Levay A, Kong LY, et al. Targeting 4-1BB costimulation to the tumor stroma with bispecific aptamer conjugates enhances the therapeutic index of tumor immunotherapy. Cancer Immunol Res 2014;2:867–77.
24. Duraiswamy J, Kaluza KM, Freeman GJ, Coukos G. Dual blockade of PD-1 and CTLA-4 combined with tumor vaccine effectively restores T-cell rejection function in tumors. Cancer Res 2013;73:3591–603.

25. Tavaré R, Wu WH, Zettlitz KA, Salazar FB, McCabe KE, Marks JD, et al. Enhanced immunoPET of ALCAM-positive colorectal carcinoma using site-specific 64Cu-DOTA conjugation. Protein Eng Des Sel 2014;27: 317–24.

26. Soret M, Bacharach SL, Buvat I. Partial-volume effect in PET tumor imaging. J Nucl Med 2007;48:932–45.

27. Knowles SM, Zettlitz KA, Tavaré R, Rochefort MM, Salazar FB, Stout DB, et al. Quantitative immunoPET of prostate cancer xenografts with 89Zr- and 124I-labeled anti-PSCA A11 minibody. J Nucl Med 2014;55:452–9.

28. Dijkers EC, Oude Munnink TH, Kosterink JG, Brouwers AH, Jager PL, de Jong JR, et al. Biodistribution of 89Zr-trastuzumab and PET imaging of HER2-positive lesions in patients with metastatic breast cancer. Clin Pharmacol Ther 2010;87:586–92.

29. Bumbaca D, Xiang H, Boswell CA, Port RE, Stainton SL, Mundo EE, et al. Maximizing tumour exposure to anti-neuropilin-1 antibody requires saturation of non-tumour tissue antigenic sinks in mice. Br J Pharmacol 2012;166:368–77.

30. Divgi CR, Welt S, Kris M, Real FX, Yeh SD, Gralla R, et al. Phase I and imaging trial of indium 111-labeled anti-epidermal growth factor receptor monoclonal antibody 225 in patients with squamous cell lung carcinoma. J Natl Cancer Inst 1991;83:97–104.

31. Boswell CA, Mundo EE, Zhang C, Stainton SL, Yu SF, Lacap JA, et al. Differential effects of predosing on tumor and tissue uptake of an 111In-labeled anti-TENB2 antibody-drug conjugate. J Nucl Med 2012;53:1454–61.

32. Muylle K, Flamen P, Vugts DJ, Guiot T, Ghanem G, Meuleman N, et al. Tumour targeting and radiation dose of radioimmunotherapy with Y-rituximab in CD20+ B-cell lymphoma as predicted by Zr-rituximab immuno-PET: impact of preloading with unlabelled rituximab. Eur J Nucl Med Mol Imaging 2015;42:1304–14.

33. Pittet MJ, Grimm J, Berger CR, Tamura T, Wojtkiewicz G, Nahrendorf M, et al. In vivo imaging of T cell delivery to tumors after adoptive transfer therapy. Proc Natl Acad Sci U S A 2007;104:12457–61.

34. Griessinger CM, Kehlbach R, Bukala D, Wiehr S, Bantleon R, Cay F, et al. In vivo tracking of Th1 cells by PET reveals quantitative and temporal distribution and specific homing in lymphatic tissue. J Nucl Med 2014;55:301–7.

35. Griessinger CM, Maurer A, Kesenheimer C, Kehlbach R, Reischl G, Ehrlichmann W, et al. 64Cu antibody-targeting of the T-cell receptor and

36. Koya RC, Mok S, Comin-Anduix B, Chodon T, Radu CG, Nishimura MI, et al. Kinetic phases of distribution and tumor targeting by T cell receptor engineered lymphocytes inducing robust antitumor responses. Proc Natl Acad Sci U S A 2010;107:14286–91.

37. McCracken MN, Gschweng EH, Nair-Gill E, McLaughlin J, Cooper AR, Riedinger M, et al. Long-term in vivo monitoring of mouse and human hematopoietic stem cell engraftment with a human positron emission tomography reporter gene. Proc Natl Acad Sci U S A 2013;110:1857–62.

38. Gschweng EH, McCracken MN, Kaufman ML, Ho M, Hollis RP, Wang X, et al. HSV-sr39TK positron emission tomography and suicide gene elimination of human hematopoietic stem cells and their progeny in humanized mice. Cancer Res 2014;74:5173–83.

39. McCracken MN, Vatakis DN, Dixit D, McLaughlin J, Zack JA, Witte ON. Noninvasive detection of tumor-infiltrating T cells by PET reporter imaging. J Clin Invest 2015;125:1815–26.

40. Yaghoubi SS, Campbell DO, Radu CG, Czernin J. Positron emission tomography reporter genes and reporter probes: gene and cell therapy applications. Theranostics 2012;2:374–91.

41. Nair-Gill E, Wiltzius SM, Wei XX, Cheng D, Riedinger M, Radu CG, et al. PET probes for distinct metabolic pathways have different cell specificities during immune responses in mice. J Clin Invest 2010;120:2005–15.

42. Li K, Zettlitz KA, Lipianskaya J, Zhou Y, Marks JD, Mallick P, et al. A fully human scFv phage display library for rapid antibody fragment reformatting. Protein Eng Des Sel 2015;28:307–16.

43. Blykers A, Schoonooghe S, Xavier C, D'Hoe K, Laoui D, D'Huyvetter M, et al. PET imaging of MMR-expressing macrophages in tumor stroma using 18F-radiolabeled camelid single-domain antibody fragments. J Nucl Med 2015;56:1265–71.

44. Rashidian M, Keliher EJ, Bilate AM, Duarte JN, Wojtkiewicz GR, Jacobsen JT, et al. Noninvasive imaging of immune responses. Proc Natl Acad Sci U S A 2015;112:6146–51.

45. Malviya G, Galli F, Sonni I, Pacilio M, Signore A. Targeting T and B lymphocytes with radiolabelled antibodies for diagnostic and therapeutic applications. Q J Nucl Med Mol Imaging 2010;54:654–76.

46. Tomblyn M. Radioimmunotherapy for B-cell non-hodgkin lymphomas. Cancer Control 2012;19:196–203.